Computational Electromagnetic Model of a Cylindrical Near-Field Antenna Test System:

Examination of Common Measurement Errors and Their Compensation

S.F. Gregson[#1], A.C. Newell[#2], G.E. Hindman[#3]

[#]NSI-MI Technologies

19730 Magellan Drive

Torrance, California, USA

[1]sgregson@nsi-mi.com, [2]anewell@nsi-mi.com, [3]ghindman@nsi-mi.com

Abstract—**This paper presents the results of a new computational electromagnetic simulation of a cylindrical near-field antenna test system. The new plane-wave spectrum representation based simulation allows many of the commonly encountered components within the range uncertainty budget to be included within the model. These terms are: range reflections, random errors and cylindrical measurement truncation. This paper presents the results of simulations that verify the utility of the cylindrical mathematical absorber reflection suppression (C-MARS) technique for compensation of their effects. Although past verifications have been done using experimental techniques this paper, for the first time, corroborates these findings using purely computational methods.**

Keywords—Cylindrical Near-Field, Computational Electromagnetic, Simulation, Cylindrical MARS.

I. INTRODUCTION

The right circular cylindrical near-field measurement system is formed from the combination of linear translation and rotation stages where the linear translation axis is parallel to the rotation axis. This enables the scanning probe to trace out a conceptual cylindrical surface [1, 2] that encloses the radiator. Here, near-field samples are taken at regular intervals across the cylindrical raster grid as illustrated in Figure 1 below. The linear and rotation axes are typically aligned to the local gravity vector which simplifies the alignment of the system and insures that the antenna under test (AUT) does not suffer a variation in orientation of the local gravity vector during an acquisition. This geometry enables complete azimuthal pattern to be obtained providing information on the wide out antenna pattern and, in principle, the front-to-back ratio. This makes the cylindrical technique appropriate for fan-beam type antenna testing where the finite length of the linear scan axis, and the inevitable truncation that introduces, has minimum impact on the accuracy of the resulting far-field data. The electromagnetic fields outside an arbitrary test antenna radiating into free-space can be expanded onto a set of orthogonal transverse electric (TE) and transverse magnetic (TM) cylindrical mode coefficients (CMC) using standard cylindrical near-field theory [1, 2]. Once obtained, these CMCs can be compensated for the directive filtering properties of the measuring probe through the use of an inversion of the cylindrical transmission formula [1] and an auxiliary characterisation of the scanning probe [2]. These probe-corrected CMCs can then be used to obtain the asymptotic far electric and magnetic fields through an efficient summation process utilising the fast Fourier transform (FFT) [1, 2].

As is the case with other forms of near-field testing, cylindrical scanning can, in many instances, have the integrity of the antenna measurement compromised in a large part by: range reflections (*i.e.* clutter), scan interval truncation and contamination by random noise which are often found to constitute some of the larger terms within the facility level uncertainty budget [2, 3]. The measurement and post-processing mode orthogonalisation and filtering technique, named Mathematical Absorber Reflection Suppression (MARS) [2, 4] has been used extensively to identify and subsequently extract measurement artifacts arising from spurious scattered fields that are admitted when antenna testing is performed in non-ideal anechoic environments including cylindrical applications where cylindrical MARS is routinely deployed [2, 5]. Underpinning the success of all forms of the C-MARS post-processing, and other mode orthogonalisation and filtering strategies [6, 7], is the behaviour of the orthogonal vector wave (mode) expansions under isometric co-ordinate translations [2, 8]. Computational electromagnetic simulations have been utilised to illustrate this behaviour and to further verify the effectiveness of the MARS processing [9], however this sort of detailed examination has not previously been extended to the cylindrical case. Thus, in order that the behaviour of the CMCs under C-MARS processing could be illustrated and examined in the absence of other spurious measurement errors, the use of a computational electromagnetic (CEM) simulation was harnessed. A computational approach was utilised, as analytical verification techniques are generally complicated by the difficulty with which closed form solutions are obtained, and even when exact solutions are available, they tend to be cumbersome and difficult to use. This is especially true for complex configurations such as those inherent to the C-MARS technique. The following sections describe the CNF simulation and present the results of a number of simulations that examine the effectiveness of the C-MARS technique in the presence of scattering, finite dynamic range and measurement area truncation [2, 3].

II. OVERVIEW OF CYLINDRICAL NEAR-FIELD ANTENNA MEASUREMENT SIMULATION ALGORITHM

Any near-field measurement can be simulated by evaluating the complex coupling coefficient between the guided-wave port on the AUT and the guided-wave port near-field probe at each point across the simulated acquisition interval for each orthogonal tangential polarisation and for every measured frequency. In principle it would be possible to

obtain these transmission coefficients from a three-dimensional electromagnetic full-wave solver and this approach would clearly have the advantage of introducing the smallest number of approximations & assumptions yielding, in principle, the most accurate measurement simulations. However, although many such solvers are available they are generally thought to be inappropriate for simulating problems such as these where each measurement point corresponds to an independent, separate simulation and each individual simulation comprises a large problem-space. This is a direct consequence of the very long processing times and the (often) large amounts of computer resources required. Hence, a switch to less general, but more efficient techniques becomes compelling [10]. Here, the plane-wave spectrum method [2, 10, 11, 12] can be harnessed to reconstruct the radiated near electric field from, for example, far-field antenna pattern data. This is a general purpose technique that underpins standard planar near-field theory and is the basis of microwave-holographic-metrology [2, 10]. The radiated near-field can be reconstructed across the surface of a right hemi-cylinder where $z > 0$ using [11],

$$\underline{E}(x,y,z) = \int\limits_{-\infty}^{\infty}\int\limits_{-\infty}^{\infty}\left[\left(\underline{\hat{u}}_x - \underline{\hat{u}}_z \frac{u}{w}\right)F_x(u,v) \right. \tag{1}$$
$$\left. + \left(\underline{\hat{u}}_y - \underline{\hat{u}}_z \frac{v}{w}\right)F_y(u,v)\right]e^{-jk_0(ux+vy+wz)}dudv$$

Here, F_x and F_y are the x- and y-polarised angular spectra, the conventional Cartesian and cylindrical coordinates are related through $x = \rho\cos\phi$, $z = \rho\sin\phi$ such that $\rho \geq 0$, $0 \leq \phi \leq 2\pi$, $-\infty \leq y \leq \infty$ [2], with the linear axis of the cylindrical system assumed aligned with the vertical y-axis of this system. Here, the reconstructed Cartesian near electric field components are sampled using a plaid monotonic and equally spaced ϕ, y, grid at which point the fields can be resolved onto a conventional cylindrical polarization basis [2] whereupon the resulting near-field data is in a form that is immediately amenable for further processing with standard cylindrical near-field to far-field transformation techniques.
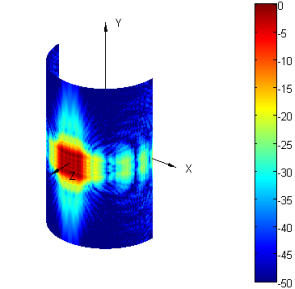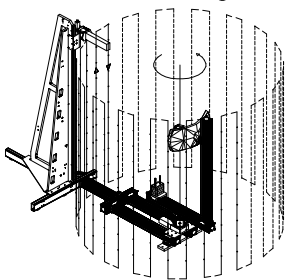

Fig. 1. Cylindrical antenna system & acquisition grid.

Fig. 2. Simulated ϕ-polarised near electric field component.

To illustrate this, Figure 2 contains the ϕ-polarized component of the near electric field of a uniformly illuminated square aperture of side 0.356 m cut in an infinitely thin perfect electric conducting (PEC) ground-plane of infinite extent.

III. SIMULATED CYLINDRICAL NEAR-FIELD MARS MEASUREMENTS & C-MARS VERIFICATION

The two orthogonal tangential near electric field components (one of which is shown in Figure 2 above) can be used to obtain the TE and TM CMCs using standard cylindrical processing [1, 2, 5] with the resulting TE modes being shown

in Figure 3. CMCs are complex numbers that are functions of frequency, the polarization index, the azimuthal index n, and the polar direction cosine γ which do not vary with any of the scanning coordinates. The study of the behaviour of these coefficients under certain transformation is the central theme of this paper. Figure 4 presents an equivalent set of CMCs as was shown in Figure 3, *i.e.* for the *same* antenna, only here the AUT has been mathematically translated to the origin of the cylindrical coordinate system [2, 5, 8]. Previously the AUT had been displaced from the origin of the measurement coordinate system in the z-axis direction by 0.36 m (14") with the distance corresponding approximately to the largest dimension of the aperture of the AUT. Here, the displacement of the AUT from the measurement origin produces a more complex phase variation of the measured cylindrical near fields. The more complex phase variation results in the need for a larger number of higher order CMCs and hence the broader distribution of modes.
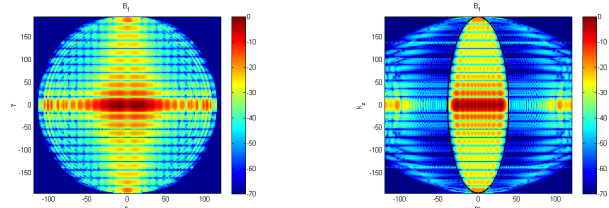

Fig. 3. CMCs for AUT when aperture displaced from origin.

Fig. 4. CMCs for AUT when aperture translated to origin.

Here, the black ellipse shown in Figure 4 denotes the highest order CMCs required by sampling theorem to represent a radiator of a given size [2] and is determined by the equality, $n^2 + (\gamma r_{t0})^2 = (k_0 r_{t0})^2$. Here, r_{t0} denotes the maximum radial extent (MRE) [2], n is the mode index and γ is the Fourier variable which is conjugate of the linear spatial variable. As a consequence of the exponential decrease in the reactive modes, any mode not within this ellipse can be filtered out without impacting the integrity of the underlying test antenna pattern function, irrespective of the complexity of that pattern. This is the power of the MARS technique.

A. Verification of Suppression of Additional Scatterers

To illustrate the effectiveness of the MARS technique, an additional spurious, source was introduced into the simulation shown above, *cf.* [2]. This took the form of an additional radiator located at a different position in space and pointing in a different direction to that of the AUT and is the reason for the apparent asymmetry in the CNF data. Prior to translating the AUT those modes associated with the AUT and the modes associated with the spurious source coexist in linear superposition. However once the AUT is translated to the origin, these mode spectra separate in the mode domain with the spurious modes shifting to larger absolute mode indices, $|n|$, as can be seen to the left and right hand sides of Figure 6. These modes can then be filtered out whereupon the MARS processed far-field pattern can be obtained from a summation of the remaining antenna modes, [2, 5]. Figure 7 below contains a plot of the far-field pattern without C-MARS processing which clearly shows the effects of the spurious source. In contrast, Figure 8 shows the equivalent far-field pattern with C-MARS processing applied where the spurious

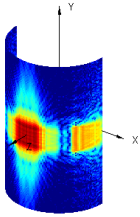signal is clearly attenuated across a wide range of elevation angles.

Fig. 5. ɸ-polarised near-field component with spurious radiator present, (50 dB scale).
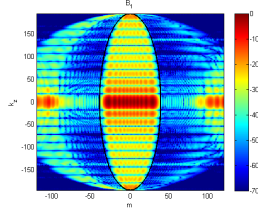

Fig. 6. CMCs of AUT translated to origin showing mode orthogonalisation, *cf.* Fig 4.

Figures 9 and 10 contain great circle azimuth amplitude and phase cuts respectively that compare these patterns to reference far-field pattern data. This provides further confirmation of the effectiveness of the filtering showing as they do a *circa* 12 dB attenuation in the vicinity of the peak of the spurious signal at 30° from boresight direction and crucially demonstrates that the remaining pattern is reliable. A similar effect can be seen in the phase patterns where the green, unfiltered results show significant ripple with the red reference and black MARS filtered traces being in very impressive agreement with one another. This simulation recreates and reconfirms results previously obtained only empirically in [5].
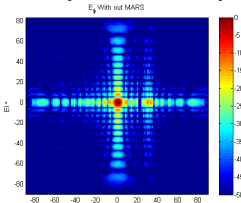
Fig. 7. Far-field pattern of AUT without C-MARS processing.
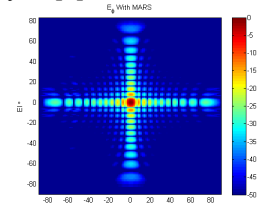
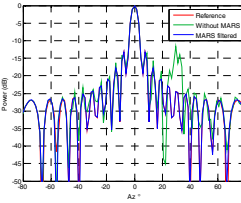Fig. 8. Far-field pattern of AUT with C-MARS processing.

Fig. 9. Azimuth amplitude cut comparing reference to patterns without & with C-MARS.
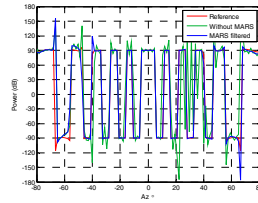

Fig. 10. Azimuth phase cut comparing reference to patterns without & with C-MARS.

As a way of further stressing the C-MARS processing, a simulation was run where the spurious signal had been orientated to point predominantly in elevation axis with the greatest effects being seen around 30° in elevation. Figure 11 presents the simulated cylindrical near-field data set, where the additional radiator is placed to the side of the AUT and is tilted up in elevation. Figure 12 presenting the corresponding far-field pattern, as obtained from regular cylindrical near-field processing showing the spurious signal. As the isometric translation of origins acts predominantly in the mode domain *n*, standard C-MARS algorithm is often viewed as being most effective with scattering artefacts that act in the azimuthal axis. The purpose of this simulation was to verify the effectiveness of standard C-MARS processing when acting on effects that exhibit themselves in the orthogonal, *i.e.* elevation, axis. Figure 13 contains an equivalent far-field false colour checkerboard plot to that shown in figure 12, only here,

standard C-MARS processing has been applied. From inspection it is evident that the spurious trail of side-lobes from the additional radiator has been very effectively suppressed.
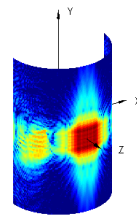

Fig. 11. ɸ-polarised electric near-field component with spurious radiator present (50 dB scale).
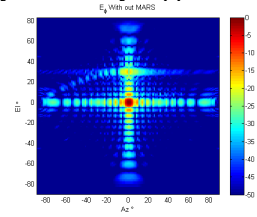

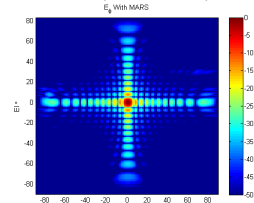Fig. 12. Far-field pattern of AUT obtained from standard CNF to FF transform.

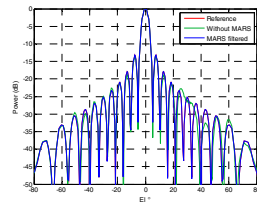Fig. 13. Far-field pattern of AUT with C-MARS processing.

Fig. 14. Elevation cuts with & without C-MARS processing.

This is further confirmed in Figure 14 where the effects of the spurious signal have been attenuated in the elevation boresight cut, particularly at +30° in elevation where the greatest effects could previously be seen. In this case the spurious signal was offset in the *x*-axis with respect to the AUT. It is the small horizontal displacement that enabled the C-MARS algorithm to succeed. Some small residuals of the spurious source do still persist however their effects are low level, *circa* -40 dB level and are very wide-out resulting from the comparatively small change in their mode structure allowing their modes to remain within the unit circle. If however, the additional spurious source had *not* been displaced by some small amount in the *x*-axis from the AUT then the C-MARS processing would have been far less effectiveness. In practice this implies that C-MARS can be effective in suppressing scattering originating from the walls of the test chamber but will be less effective in compensating from scatterers located along the vertical centre-line of the test chamber. However for that specific case, the more recent development of two-dimensional C-MARS can be used [13]. As cylindrical measurements are typically deployed to measure antennas with higher gain in the elevation axis, this means that there is generally less power radiating in wide elevation angles meaning that lower field intensity illuminates these parts of the test environment.

To construct a more demanding test case, the rectangular aperture was replaced with the aperture illumination function of a known measured antenna. As before, an additional spurious source was introduced, of equal intensity to that of the AUT but orientated to radiation predominantly at an azimuth angle of -30°. Figures 15 and 16 show the far-field azimuth amplitude and phase plots respectively for the case where regular CNF processing has been used. Here, the black trace denotes the error contaminated pattern with the blue trace representing the reference unperturbed pattern. Figure 17 and 18 contain equivalent amplitude and phase patterns however here C-MARS processing has been used to suppress the spurious signal. From inspection of these plots, for both the

amplitude and phase patterns the agreement attained between the reference and compensated patterns is very encouraging, further confirming the reliability of the C-MARS technique.
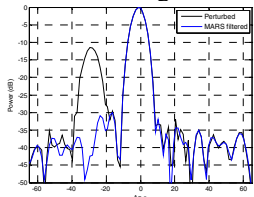

Fig. 15. Comparison of azimuth amplitude cuts comparing processed & perturbed patterns.
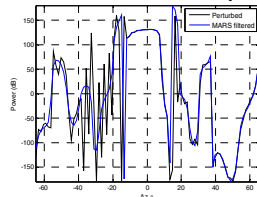

Fig. 16. Comparison of azimuth phase cuts comparing processed & perturbed patterns.
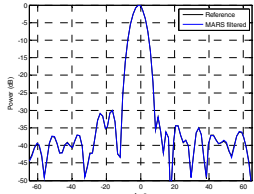

Fig. 17. Comparison of azimuth amplitude cuts comparing reference & perturbed patterns with C-MARS processing.
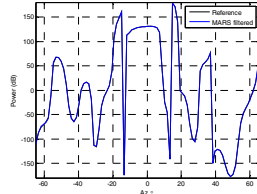

Fig. 18. Comparison of azimuth phase cuts comparing reference and perturbed patterns with C-MARS processing.

B. Verification of Improvement in Signal to Noise Ratio

Previous studies have shown that C-MARS processing is able to increase the effective far-field system signal to noise ratio (SNR) [2]. This is possible as noise power is distributed equally across the mode spectra whereas modes associated with the AUT are bounded within the mode domain. As the translation of origins has the effect of reducing the power distribution of modes associated with the AUT to a minimum, an effective increase in the SNR is typically achieved. This increase in SNR is separate and in addition to the transform gain that also aids with system SNR in the far-field [2]. As a further verification of the new CNF CEM model, this feature of C-MARS was explored. Figure 19 shows the baseline CNF data plotted as a false colour checkerboard plot, cf. Figure 2. Figure 20 shows the same data, only here with the addition of random noise. In this case, noise was added such that the amplitude was normally distributed with a standard distribution of 2 standard deviations (2σ) about a mean value of -46 dB with a uniformly distributed phase error. This corresponds closely with what is seen in practice. Within modern receivers and vector network analysers (VNA), phase is recovered from a ratio of two measurements each possessing nominally the same error distribution. The distributions approximately cancel results in the uniform 360° phase distribution encountered [2]. Here, the mean amplitude noise signal level was chosen as this is a nominal value for a chamber lined with *poorly* performing 12" pyramidal absorber, *i.e.* selecting a "bad" chamber constitutes a good test case. The effect this has on the CNF data can be seen illustrated in Figure 20. Figure 21 presents the CMCs for the AUT for the case in the absence of noise whereas Figure 22 contains an equivalent plot for the noise contaminated case. Here, power contained in spurious random noise outside the black ellipse corresponds to CMCs that are excluded by the C-MARS processing. The far-field pattern obtained using standard cylindrical processing can be seen presented in Figure 23 which clearly shows an increase in the background noise level especially in the regions off the

principal planes over the uncontaminated result *e.g.* Figure 8. Conversely, the equivalent C-MARS processed, *i.e.* filtered, result is presented in Figure 24.
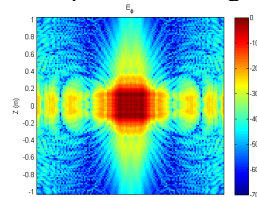

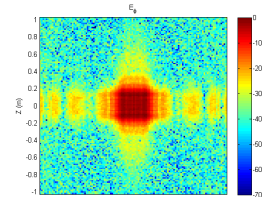Fig. 19. φ-polarised electric near-field component without spurious random signal added.

Fig. 20. φ-polarised electric near-field component with spurious random signal added.
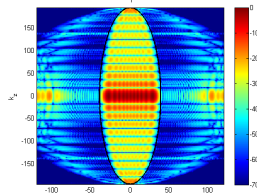

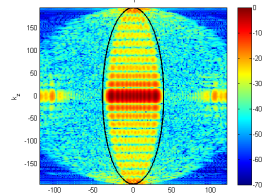
Fig. 21. CMCs of AUT in absence of noise.

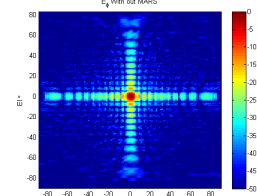Fig. 22. CMCs of AUT in presence of noise.

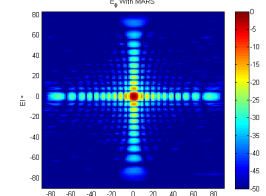Fig. 23. Far-field pattern of AUT without C-MARS processing.

Fig. 24. Far-field pattern of AUT with C-MARS processing.

From comparison of Figure 24 with a noise free result, that of say Figure 8, it is clear that C-MARS processing has significantly reduced the background noise level. By way of further confirmation, the root mean square (RMS) difference level between the reference and noise contaminated result was computed and found to be -49.9 dB. When the RMS difference level was computed between the reference and C-MARS processed noise contaminated result the level was found to be -57.5 dB which corresponds to an overall improvement in signal to error level of more than 7.5 dB. This is an encouraging result. Here, the comparisons are made in the far-field meaning that this improvement in the RF link budget is in addition to any improvement yielded by the gain of the cylindrical near-field to far-field transform.

C. Verification of Suppresion of 2nd Order Truncation Effects

The third distinct capability of C-MARS is the ability to suppress the second-order truncation effect, or Gibbs ripple [2, 10]. Cylindrical mode truncation is introduced by presence of a sharp discontinuity at the boundary of the finite sampling interval. This boundary is a consequence of the finitely long linear-axis and necessitates the use of a larger number of higher order CMCs to represent this non-physical discontinuous behaviour of the measured near electric fields. As C-MARS processing removes higher order CMCs this means that it also suppresses Gibbs like phenomena. In order that this could be examined more closely, a number of simulations were constructed with linear spans of 2.0 m, 1.4 m, and 1.0 m. These correspond to a maximum valid elevation pattern angle

[2, 10] of *circa* 68°, 57° and 44° respectively. Each CNF data set was transformed to the far-field using the standard cylindrical near-field to far-field transformation (Figure 25, 27, 29 respectively) and again with C-MARS processing being applied (Figures 26, 28, 30 respectively). The resulting elevation boresight pattern cuts were then compared and the RMS difference levels calculated.
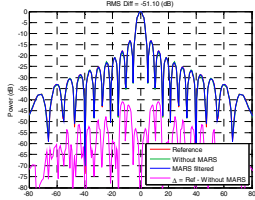

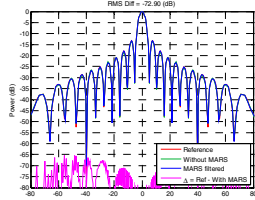Fig. 25. 2.0 m truncation test Δ computed without MARS.

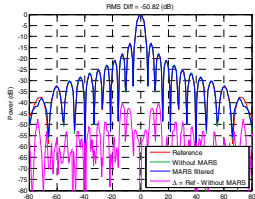Fig. 26. 2.0 m truncation test Δ computed with MARS.

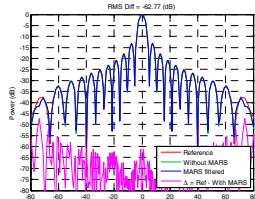Fig. 27. 1.4 m truncation test Δ computed without MARS.

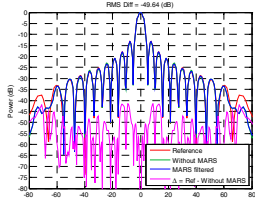Fig. 28. 1.4 m truncation test Δ computed with MARS.

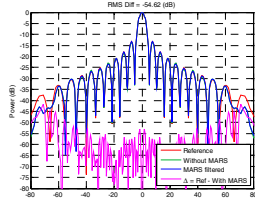Fig. 29. 1.0 m truncation test Δ computed without MARS.

Fig. 30. 1.0 m truncation test Δ computed with MARS.

In figures 25 to 30, the red trace denotes the reference far-field pattern, the green trace is the truncated far-field pattern obtained using standard cylindrical processing, the blue trace denotes the C-MARS processed result and the magenta trace represents the difference level when expressed in dB form, [2]. For figures 25, 27 and 29 the difference level was calculated between the reference and the far-field pattern without C-MARS processing whereas for figures 26, 28 and 30 the difference was calculated between the reference and the C-MARS processed patterns. In each case, the patterns show a significant improvement in the degree of agreement within the valid elevation angle for the case where C-MARS processing has been applied. This is expected as, *cf.* Figure 29, the green (without MARS) trace can be seen to be most obviously different to the blue (with MARS) trace mainly in the vicinity of the peaks of the side-lobes. This result is also confirmed by comparing the RMS difference levels obtained with and without applying MARS processing. Here, there was a 20 dB, 12 dB and 5 dB improvement in the RMS difference levels respectively for the 2.0 m, 1.4 m and 1.0 m cases. The degradation with decreasing span is a consequence of the increasing impact of the first order truncation effect which is revealed by the greater differences for wide-out pattern angles. Although not shown due to the constraints of space, the azimuth patterns do show some variation with linear span, which is a natural consequence of the anti-reductionist

relationship that exists between the near- and far-fields, although that difference is small.

IV. SUMMARY AND CONCLUSIONS

This paper has presented the results of a new cylindrical near-field measurement simulation that has, for the first time, enabled the effectiveness of C-MARS processing to be verified computationally. Crucially, within sections IIIa, IIIb and IIIc the ability of C-MARS processing to suppress spurious signals, improve system dynamic range and to lessen the effects of the second order truncation effect have been demonstrated. Previously, it has only been possible to verify these observations experimentally. This simulation has also been used to verify that: 1) CMCs resulting from scattering are displaced to higher order modes with AUT modes being shifted to lower order modes once the AUT is mathematically translated back to the origin of the measurement coordinate system, 2) the amount of separation between mode distributions associated with scattering and those associated with the AUT increases as the displacement increases, 3) C-MARS processing is capable of suppressing scattering providing that the magnitude of the displacement is sufficiently large. This behaviour has also been observed in spherical mode based expansions, *cf.* [2, 8]. As shown above, the CEM model has been able to provide further confirmation of the effectiveness of the C-MARS processing, showing that it can be used with a very high degree of confidence.

REFERENCES

[1] A.D. Yaghjian, "Near-Field Antenna Measurements On a Cylindrical Surface: A Source Scattering Matrix Formulation", NBS Technical Note 696, 1977.

[2] C.G. Parini, S.F. Gregson, J. McCormick, D. Janse van Rensburg "Theory and Practice of Modern Antenna Range Measurements", IET Press, 2014, ISBN 978-1-84919-560-7.

[3] A.C. Newell, "Error Analysis Techniques for Planar Near-field Measurements", IEEE Transactions on Antennas and Propagation, vol. AP-36, pp. 754-768, June 1988.

[4] G.E. Hindman, A.C. Newell, "Reflection Suppression in a large spherical near-field range", AMTA, Newport, RI, October. 2005.

[5] S.F. Gregson, A.C. Newell, G.E. Hindman, "Reflection Suppression in Cylindrical Near-Field Antenna Measurement Systems – Cylindrical MARS", AMTA, Salt Lake City, UT, November, 2009.

[6] O.M. Bucci, G. D'Elia, M.D. Migliore, "A General and Effective Clutter Filtering Strategy in Near-Field Antenna Measurements", IEEE Proc.-Microwave Antennas and Propagation, Vol. 151, No. 3, June 2004.

[7] D.W. Hess, "The IsoFilter™ Technique: Isolating an Individual Radiator from Spherical Near-Field Data Measured in a Contaminated Environment", EuCAP 2007.

[8] S.F. Gregson, A.C. Newell, G.E. Hindman, "Behaviour of Orthogonal Wave Functions And The Correction of Antenna Measurements Taken in Non-Anechoic Environments", LAPC, November 2013.

[9] S.F. Gregson, A.C. Newell, G.E. Hindman, "Examination of Far-Field Mathematical Absorber Reflection Suppression Through Computational Electromagnetic Simulation", International Journal of Antennas and Propagation, Special Issue on Recent Advances in Near-Field to Far-Field Transformation Techniques, March 2012.

[10] S.F. Gregson, J. McCormick, C.G. Parini, "Principles of Planar Near-Field Antenna Measurements", IET Press, UK, 2007, ISBN 978-0-86341-736-8.

[11] R.H. Clarke, J. Brown, "Diffraction Theory and Antennas", Ellis Horwood Ltd., 1980.

[12] A.C. Newell, S.F. Gregson, "Estimating the Effect of Higher Order Modes in Spherical Near-Field Probe Correction", AMTA, October 2012,

[13] S.F. Gregson, A.C. Newell, G.E. Hindman, "Extending Cylindrical Mathematical Absorber Reflection Suppression To Further Reduce Range Scattering Errors", LAPC, November 2012.